Communications in Physics, Vol. 36, No. 1 (2026), pp. 57-70
DOI: https://doi.org/10.15625/0868-3166/23283

Facile shape control of $GdPO_4.H_2O:Tb^{3+}$ by solvothermal method using di/polyethylene glycol as soft template

Nguyen Thanh Huong[1,†], **Pham Thi Lien**[1], **Hoang Thi Khuyen**[1], **Nguyen Thi Ngoc Anh**[1], **Do Khanh Tung**[1], **Nguyen Vu**[1], **Dinh Manh Tien**[1] **and Nguyen Thanh Binh**[2]

[1]*Institute of Materials Sciences, Vietnam Academy of Science and Technology, 18 Hoang Quoc Viet Road, Nghia Do, Hanoi 100000, Vietnam*

[2]*Institute of Physics, Vietnam Academy of Science and Technology, 10 Dao Tan, Giang Vo, Hanoi 11108, Vietnam*

E-mail: [†]nthuongims@gmail.com

Received 9 August 2025
Accepted for publication 13 November 2025
Published 5 March 2026

Abstract. *Tb^{3+}-doped $GdPO_4{\cdot}H_2O$ phosphors were synthesized with wire-, rod-, and particle-like morphologies using a solvothermal method. This was achieved by varying the reaction solvent between diethylene glycol (DEG) and polyethylene glycol (PEG) of different molecular weights. The crystal structure, morphology, and photoluminescence (PL) properties were characterized using X-ray diffraction (XRD), field-emission scanning electron microscopy (FESEM), and PL spectroscopy. The emission spectra showed the characteristic green luminescence of Tb^{3+} ions, with transition from the $^5D_4 \rightarrow {}^7F_j$ (J = 6, 5, 4, 3) at 489, 543, 586, and 620 nm, respectively. Systematic analysis revealed a strong correlation between material morphology, crystal structure, and luminescence efficiency. The sample with a nanoparticle morphology, synthesized at 100 ˚C in a PEG 8000 medium, exhibited the highest PL intensity. It displayed a dominant green emission at 543 nm ($^5D_4 \rightarrow {}^7F_5$) and sharp, well-defined emission bands. These findings confirm that a solvent-mediated morphology control strategy is effective for optimizing the luminescence performance of $GdPO_4$-based phosphors.*

Keywords: $GdPO_4{\cdot}H_2O:Tb^{3+}$; solvothermal method; PEG; DEG; morphology control; photoluminescence.

Classification numbers: 78.55.Kz; 78.55.Hx; 82.20.Yn; 87.17.Pq.

1. Introduction

Luminescent nanomaterials based on rare-earth-doped phosphates have garnered significant scientific attention for their unique optical properties, which include long fluorescence lifetimes, high luminescence efficiency, large Stokes shifts, narrow emission bands, and excellent photostability [1–4]. These attributes make them highly suitable for a wide range of applications, such as bioimaging, sensing, and advanced displays [5–8].

Among various lanthanide-containing host compounds such as phosphates, vanadates, and fluorides, lanthanide phosphate ($LnPO_4$) nanomaterials are particularly promising due to their exceptional thermal stability, chemical durability, good aqueous dispersibility, and environmental friendliness [9–12]. When doped with activator ions like Eu^{3+} or Tb^{3+} , these materials exhibit strong, narrow-band luminescence, and remarkable irradiation stability, which are ideal for biomedical applications [13–15].

The $GdPO_4:Tb^{3+}$ system is of great significance for molecular biology, where it can be used for the labeling of viruses, bacteria, and cancer cells [16–23]. While several synthesis methods exist, including co-precipitation [24], sol-gel [8], and microwave-assisted techniques [25], the hydrothermal synthesis method [13], is particularly effective for achieving precise control over particle size and morphology, yielding highly crystalline products [11, 26].

A material's optical and chemical properties are critically dependent on size, shape, and crystal structure [3, 5, 27]. Therefore, a key challenge in optimizing the luminescence performance of Tb^{3+} -activated phosphates is to precisely control their morphology [4, 13, 28, 29]. This work addresses this challenge by exploring a solvent-mediated approach.

In this study, $GdPO_4{\cdot}H_2O:Tb^{3+}$ phosphors nanoparticles were synthesized using the solvothermal method with diethylene glycol (DEG) and polyethylene glycol (PEG) as shape-controlling solvents. We systematically investigated the effects of these solvents on the morphology, crystal structure, and photoluminescence performance of the synthesized materials to establish a clear correlation between these factors and materials' luminescence efficiency.

2. Experiment

The chemicals used in the synthesis were high-purity reagents: Gadolinium(III) nitrate hexahydrate ($Gd(NO_3)_3{\cdot}6H_2O$, 99.9%); Terbium(III) nitrate hexahydrate ($Tb(NO_3)_3{\cdot}6H_3O$, 99.999%); Ammonium dihydrogen phosphate ($NH_4H_2PO_4$, 99.999%); Diethylene glycol ($(HOCH_2CH_2)_2O$, 99%) (DEG); and Poly(ethylene glycol) (PEG) ($H(OCH_2CH_2)_nOH$) with average molar masses of 200 (PEG 200) and 8,000 (PEG 8000) were purchased from Sigma-Aldrich. Ethanol (C_2H_5OH, $\geq$99.8%) was obtained from Merck. Deionized (DI) water was used throughout the synthesis of the $GdPO_4{\cdot}H_2O:Tb^{3+}$ materials.

Materials Synthesis: $GdPO_4{\cdot}H_2O:Tb^{3+}$ nanostructures were synthesized using a solvothermal method. Gadolinium(III) nitrate hexahydrate ($Gd(NO_3)_3{\cdot}6H_2O$) and terbium(III) nitrate hexahydrate ($Tb(NO_3)_3{\cdot}6H_3O$) were first dissolved in 10 mL of diethylene glycol (DEG) under ultrasonication to form a clear solution, the molar ratio of Tb^{3+}/Gd^{3+} is 0.07. Separately, ammonium dihydrogen phosphate ($NH_4H_2PO_4$) was dissolved in 10 mL of DEG using vortex mixing, the molar ratio of PO_4^{3-}/RE is 2.

The phosphate solution was then placed in a 50 mL round-bottom flask, and the nitrate solution was added dropwise while stirring at room temperature for 30 min. The resulting mixture was

transferred into a Teflon-lined stainless-steel autoclave for solvothermal treatment at 100 °C for 24 hours. The final product was collected via centrifugation, washed multiple times with deionized water and ethanol, and dried at 60 °C for 24 hours (Scheme 1). This procedure was repeated using poly(ethylene glycol) (PEG) with average molecular weights of 200 (PEG 200) and 8,000 (PEG 8000) as alternative solvents to DEG.

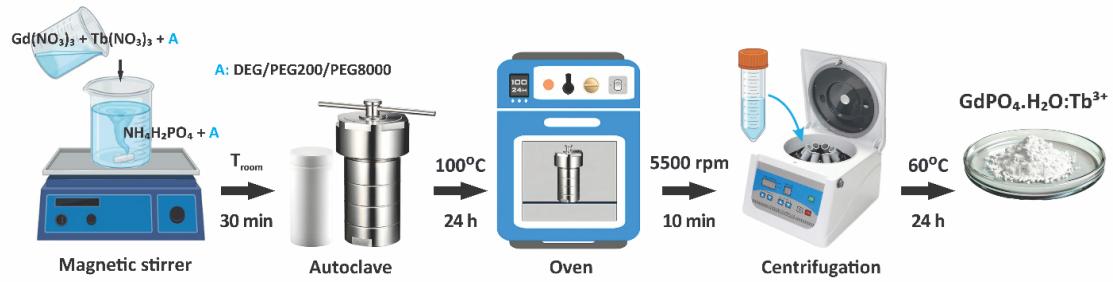

Scheme 1. Schematic diagram of synthesis process of $GdPO_4{\cdot}H_2O{:}Tb^{3+}$.

Characterization: The morphology and particle size of the synthesized samples were examined using Field-Emission Scanning Electron Microscopy (FESEM) (Hitachi S4800) and high-resolution transmission electron microscopy (HRTEM) (JEM 2100, JEOL). Crystal structure was identified by X-ray Diffraction (XRD) (D8 ADVANCE, Bruker). Zeta potential measurements were performed by Dynamic Light Scattering (Zetasizer Nano ZS, Malvern, UK). Raman spectra were recorded using a Horiba XploRA PLUS Raman microscope. Fourier Transform Infrared (FTIR) spectroscopy was performed on a Nicolet iS10 instrument (Thermo Scientific, USA). Finally, Photoluminescence excitation (PLE) spectra were measured with a high resolution spectrofluorometer (FL 3-22 HORIBA), photoluminescence spectra were recorded with a high-resolution spectrometer (Microspec-2356, USA) using 355 nm laser diode (Teem Photonics, Grenoble, France) excitation and the fluorescence lifetime measurements were carried out using an FLS1000 Photoluminescence Spectrometer (Edinburgh Instruments, UK).

3. Results and discussion

3.1. Morphological and structure characteristics

FESEM Analysis: In this study, the morphology of $GdPO_4{\cdot}H_2O{:}Tb^{3+}$ was effectively controlled by varying the solvent in the solvothermal synthesis. Diethylene glycol (DEG), low–molecular–weight polyethylene glycol (PEG 200) and high–molecular–weight polyethylene glycol (PEG 8000) were used to produce nanowires, nanorods, and nanoparticles, respectively. The morphological features of the resulting materials were examined using field-emission scanning electron microscopy (FESEM). A schematic of the synthesis route and the corresponding FESEM images for the $GdPO_4{\cdot}H_2O{:}Tb^{3+}$ samples synthesized at 100 °C using DEG, PEG 200, and PEG 8000 as solvents are presented in Fig. 1.

FESEM observations revealed clear morphological differences among the three $GdPO_4 \cdot H_2O{:}Tb^{3+}$ samples. The product synthesized with DEG consisted of slender nanowires, hundreds of nanometers in length with a diameter of 10–15 nm. The PEG 200 sample, in contrast, displayed short nanorods with a lower aspect ratio, approximately 150–200 nm in length

and 40–50 nm in width. The PEG 8000-mediated sample, prepared with a high-molecular-weight, high-viscosity polymer, predominantly comprised nearly spherical nanoparticles with uniform diameters of 30–60 nm. These results confirm that the different solvents act as soft templates, directing the formation of distinct particle morphologies.

The observed morphology variations are attributed to differences in the physicochemical properties of the solvents. DEG with low viscosity and weak coordination to Gd_3^+ ions facilitated one-dimensional oriented crystal growth, resulting in the formation of nanowires. Conversely, the intermediate viscosity and chain length of PEG 200 partially suppress crystal growth along specific crystallographic directions, thus favoring the formation of nanorods. In the case of PEG 8000, its long polymer chains and high viscosity significantly reduced the diffusion of ions, which inhibited anisotropic growth and promoted isotropic crystallization, leading to uniform spherical nanoparticles.

These results demonstrate that the solvent acts as both a reaction medium and a morphology-directing agent, providing a simple and effective method to tailor the particle shape and optimize the functional properties of $GdPO_4$-based phosphors.

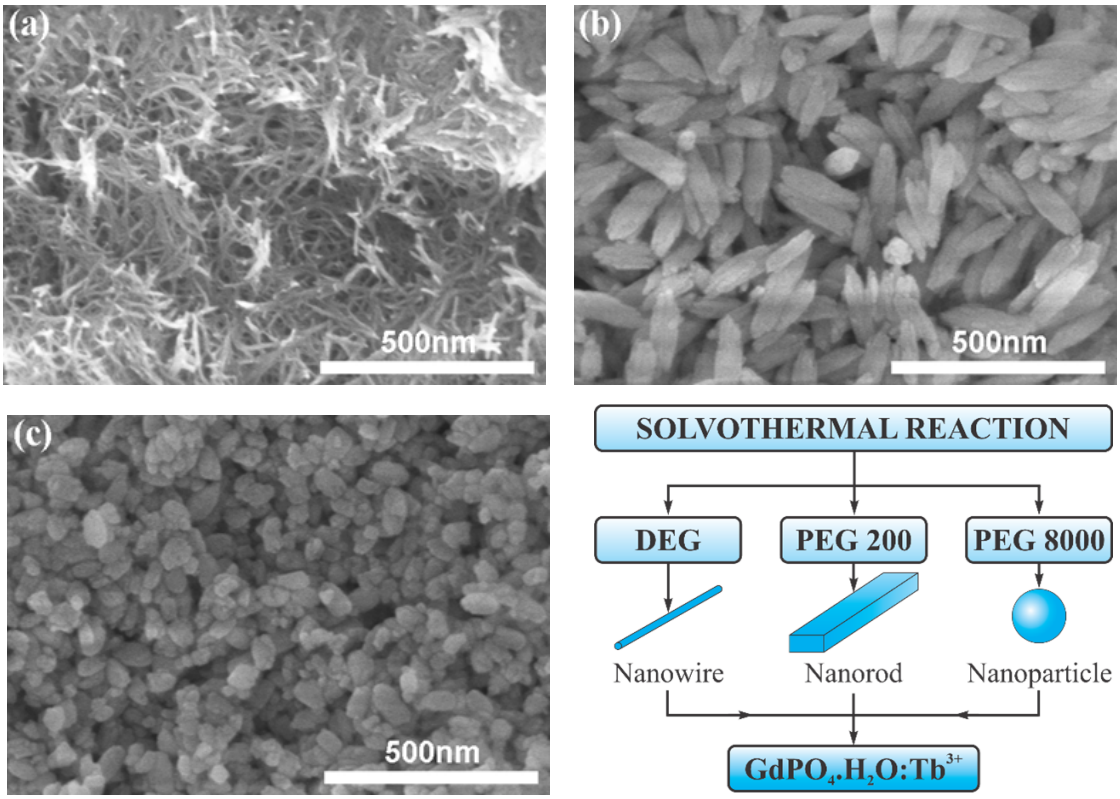

Fig. 1. Synthesis scheme and FESEM images of $GdPO_4 \cdot H_2O:Tb^{3+}$ synthesized with different solvents DEG (a), PEG 200 (b) and PEG 8000 (c).

Zeta Potential Analysis: The colloidal stability of the $GdPO_4 \cdot H_2O:Tb^{3+}$ particle suspension was evaluated by measuring its zeta potential. As shown in Fig. 2, the sample synthesized

in the presence of PEG 8000 exhibited a zeta potential of −35 mV. This highly negative value confirms excellent colloidal stability, as it indicates a strong electrostatic repulsion between the nanoparticles that prevents aggregation.

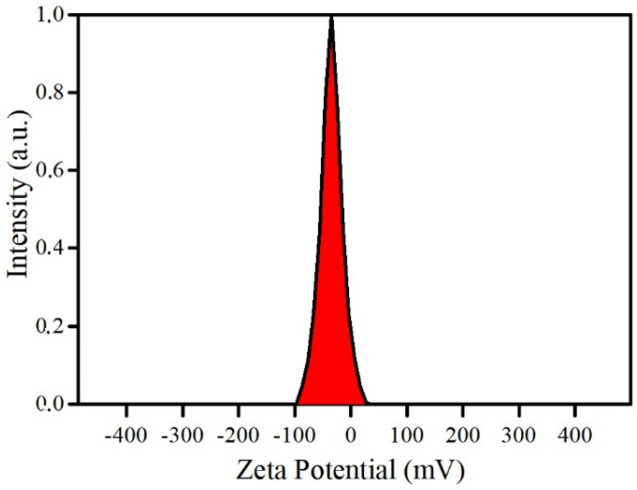

Fig. 2. Zeta potential of nanoparticle $GdPO_4 \cdot H_2O{:}Tb_3{}^+$ synthesized with PEG 8000 solvent.

The negative surface charge is likely originated from phosphate groups (PO_4^-) at the particle surface in an aqueous medium. Such a high negative zeta potential suggests long-term dispersion stability, which is a critical characteristic for practical applications in luminescent materials, sensors, and other colloidal nanomaterial systems, as it ensures homogeneity, long-term dispersion stability, and minimal particle agglomeration.

X-ray diffraction: X-ray diffraction (XRD) measurements were performed on $GdPO_4{\cdot}H_2O{:}Tb^{3+}$ samples synthesized with different solvents (DEG, PEG 200, and PEG 8000) to determine the structural configuration of the materials.

The X-ray diffraction (XRD) patterns for the $GdPO_4{\cdot}H_2O{:}Tb^{3+}$ samples synthesized with different soft templates (DEG, PEG 200, and PEG 8000) are shown in Fig. 3. All samples exhibited diffraction peaks that matched well with the standard PDF# 00-039-0232 for $GdPO_4$ with a hexagonal close-packed structure, confirming the successful formation of the desired crystalline phase in all the synthesized samples. The absence of any impurity peaks corresponding to Gd_2O_3, $TbPO_4$ indicates that Tb^{3+} ions were effectively doped into the $GdPO_4$ crystal lattice without forming separate secondary phases. Moreover, in Fig. 3b, the enlarged view of the (102) diffraction peak shows slight shift toward higher 2θ angles for all samples. This phenomenon can be attributed to the difference in ionic radii, which results in lattice distortion. The ionic radius of Gd^{3+} is approximately 1.053 Å, whereas that of Tb^{3+} is about 1.040 Å which is slightly smaller than the host it replaces. The substitution of a smaller ion decreases the lattice constant and, critically, the interplanar spacing (d). According to Bragg's diffraction law,

$$2d \sin\theta = n\lambda,$$

and in this case where n and λ are constant, a decrease in d must result in a corresponding increase in the diffraction angle 2θ, leading to the XRD peaks shifting toward the higher angle position.

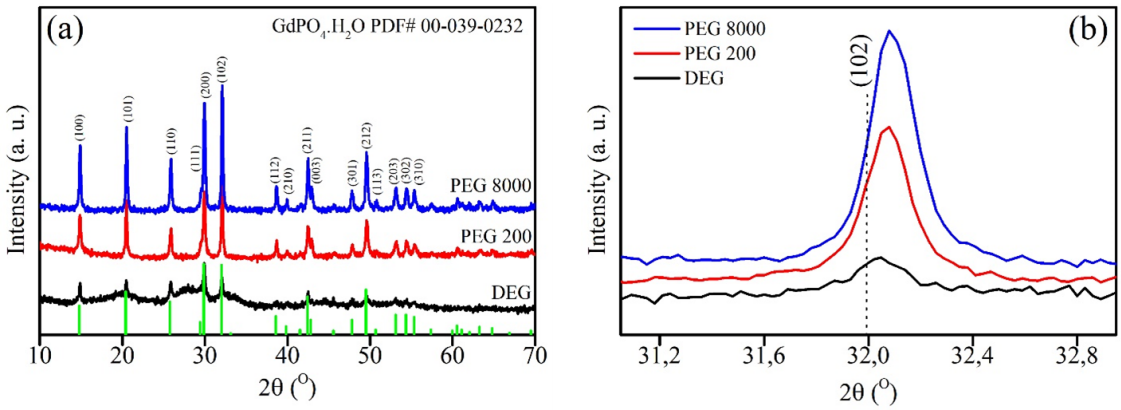

Fig. 3. XRD patterns of $GdPO_4{\cdot}H_2O:Tb^{3+}$ synthesized using different solvents (DEG, PEG 200, and PEG 8000) (a), and the enlarged view of the (102) diffraction peak region (b).

In addition, the identical Tb^{3+} concentration in all samples is evidenced by the similar peak shifts observed in their diffraction patterns.

The choice of solvent significantly influenced the material's crystallinity. Both the samples synthesized with PEG 200 and PEG 8000 showed sharp and narrow diffraction peaks, reflecting good crystallinity. Notably, the sample synthesized with PEG 8000 exhibited the sharpest and most intense peaks, suggesting the formation of highly crystalline, well-developed crystals. In contrast, the sample synthesized with PEG 200 displayed lower diffraction intensity and less defined peaks.

It is worth noting that the sample synthesized with DEG displayed a high background and broad, weak peaks, which are characteristic of poor crystalline or nearly amorphous materials. The sharp and narrow peaks observed in the samples synthesized with PEG 200 and PEG 8000 indicate a good degree of crystallization.

The average crystallite size of the $GdPO_4{\cdot}H_2O:Tb^{3+}$ nanostructures was calculated using the Debye-Scherrer formula on the most prominent diffraction peak:

$$D_{aver.} = \frac{K\lambda}{\beta \cos(\theta)},$$

where $D_{aver.}$ is the average crystallite size (nm); K is the Scherrer constant–shape factor (typically taken as ~0.9); λ is the wavelength of the X-ray source used (Cu Kα = 0.15406 nm); β is the full width at half maximum (FWHM) of the peak in radians; and θ is the Bragg diffraction angle (half of the 2θ angle at the diffraction peak position).

The Scherrer method is most reliable for calculating the crystalline size of materials with dimensions below 100 nm. For improved accuracy, it is best to use sharp, single diffraction peaks with 2θ angles in the range of 30° to 50°. This range is optimal because the peaks are less affected by background noise, maintain more symmetric shapes, and are subjected to minimal instrumental error. These factors are crucial for the precise determination of the full width at half maximum (β) value. In contrast, peaks at angles below 30° can be distorted or asymmetric, making accurate peak shape analysis difficult. Conversely, peaks at angles above 50° are more significantly affected by

instrumental error, internal strain, and lattice defects, which can cause peak broadening that does not accurately reflect crystallite particle size alone.

Therefore, in this study, to ensure the highest possible accuracy, the most intense diffraction peak for $GdPO_4 \cdot H_2O{:}Tb_3{}^+$ was chosen for the calculation. This peak, located at $2\theta = 32^\circ$ and corresponding to the (102) crystal plane, falls within the optimal range. The results of the crystallite size calculations are summarized in Table 1.

Table 1. Average crystallite size of $GdPO_4 \cdot H_2O{:}Tb_3{}^+$ samples with different solvents.

Samples	$GdPO_4 \cdot H_2O{:}Tb_3{}^+$ (PEG 8000)	$GdPO_4 \cdot H_2O{:}Tb_3{}^+$ (PEG 200)	$GdPO_4 \cdot H_2O{:}Tb_3{}^+$ (DEG)
$D_{aver.}$ (nm)	94	74.3	49.2

This result indicates that PEG 8000 plays a crucial role in controlling crystallization. Tts high viscosity and strong polymer–ion interactions effectively regulate the kinetics of crystallite growth, leading to a higher degree of crystallinity.

High-Resolution Transmission Electron Microscopy (HRTEM) analysis confirmed that the $GdPO_4{\cdot}H_2O$ particles have a uniform size distribution of 30–60 nm, which is consistent with the particle sizes estimated from FESEM measurements (Fig. 4a). High-resolution images clearly show well-defined lattice fringes, corresponding to interplanar spacings of 0.29 nm for the (102) plane, 0.33 nm for the (110) plane, 0.45 nm for the (101) plane, and 0.59 nm for the (100) plane (Fig. 4b). These measured values align well with those calculated from XRD data for hexagonal $GdPO_4{\cdot}H_2O$. This consistency verifies the high crystallinity, structural integrity, and homogeneity of the materials, with no evidence of impurity phases or significant lattice distortions.

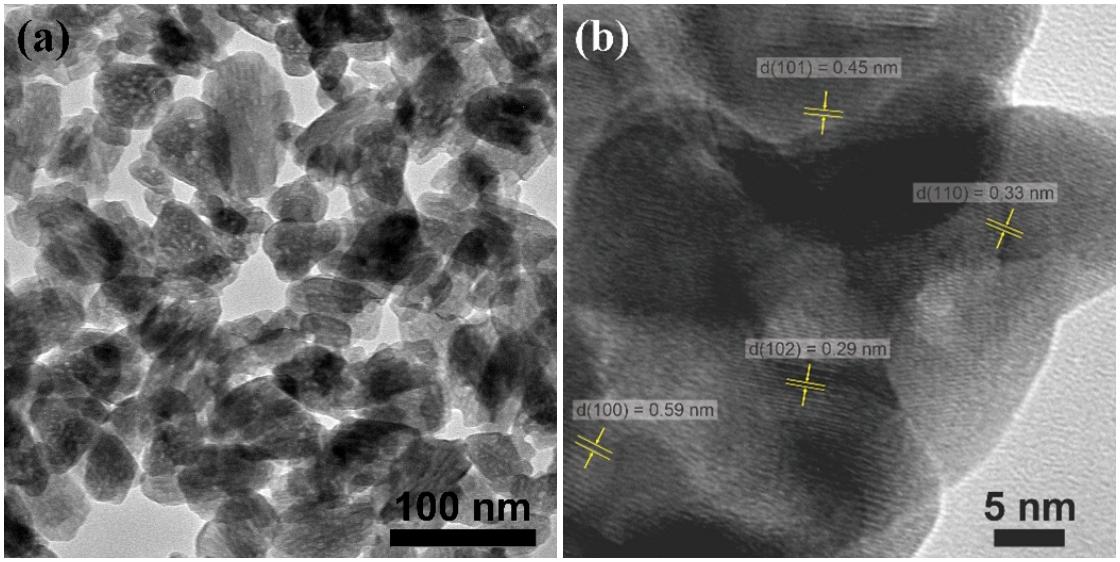

Fig. 4. HRTEM images of nanoparticle $GdPO_4{\cdot}H_2O{:}Tb^{3+}$ synthesized with PEG 8000 solvent.

The Raman spectrum of $GdPO_4{\cdot}H_2O{:}Tb^{3+}$ exhibits several distinct bands in different spectral regions, each corresponding to the characteristic vibrational modes of the crystal lattice (Fig.

5). The low-frequency region below ~200 cm^{-1} is assigned to lattice modes, which are translational vibrations of the rare-earth ions (Gd^{3+}/Tb^{3+}). These modes reflect the long-range structural order of the material. Bands observed in the 200–300 cm^{-1} range are associated with vibrational modes, involving the bending of the metal-oxygen-phosphate (M–O–P) linkage between PO_4^{3-} tetrahedra and rare-earth cations, providing insight into the strength and nature of M–O–P bonding. The 400–500 cm^{-1} region corresponds to the symmetric and asymmetric O–P–O bending modes within the phosphate groups, confirming the preservation of the tetrahedral geometry. The high-frequency region at 800–1000 cm^{-1} is dominated by the symmetric (ν_1) and asymmetric (ν_3) P–O stretching vibrations, which are characteristic of well-ordered PO_4^{3-} units. The consistency of these vibrational features with those reported for crystalline $GdPO_4{\cdot}H_2O$ confirms that the incorporation of Tb^{3+} does not disrupt the phosphate framework. This result supports the conclusions of high crystallinity and structural stability of the material derived from the XRD and HRTEM analyses.

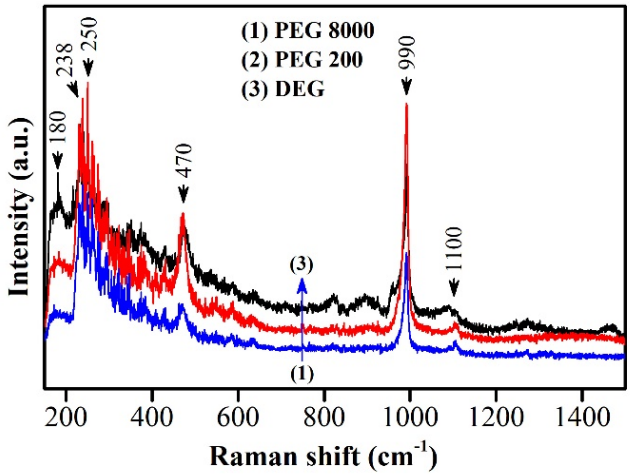

Fig. 5. Raman spectra of $GdPO_4{\cdot}H_2O:Tb^{3+}$ synthesized with different solvents DEG, PEG 200 and PEG 8000.

The Fourier-Transform Infrared (FTIR) spectra of $GdPO_4{\cdot}H_2O:Tb^{3+}$ nanostructures synthesized with different solvents (DEG, PEG 200, PEG 8000) reveal key differences in surface composition and structural integrity across the different morphologies. All three samples—nanowires, nanorods, and nanoparticles—exhibit characteristic vibrational bands corresponding to both the phosphate group and surface-bound species, confirming the successful formation of the $GdPO_4$ lattice. All three morphologies show strong absorption bands consistent with the phosphate host material. The bands at 1015 cm^{-1} and 921 cm^{-1} are assigned to the symmetric (ν_1) and asymmetric (ν_3) P-O stretching modes of the $PO_{43}{}^{-}$ tetrahedra, while the lower-frequency bands at 616 cm^{-1} and 547 cm^{-1} correspond to the O-P-O bending modes (ν_4). The consistency of these bands across all samples confirms that the fundamental phosphate structure remains intact, regardless of the synthesis solvent [28]. However, significant differences were observed in the high-frequency region, which are related to surface chemistry: The nanowire sample shows broad absorption

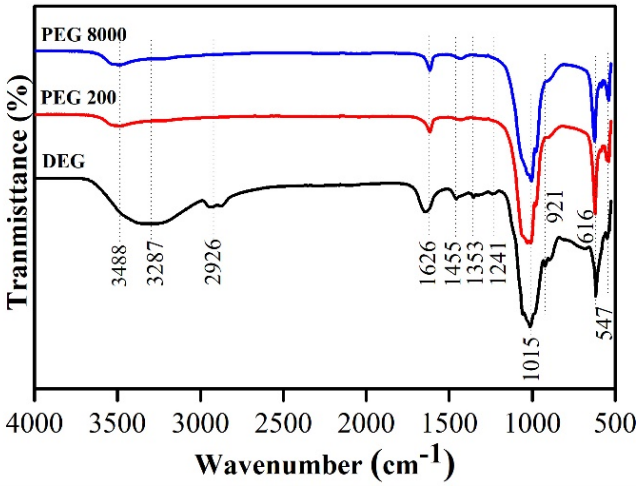

Fig. 6. FTIR spectra of $GdPO_4{\cdot}H_2O{:}Tb^{3+}$ synthesized with different solvents DEG, PEG 200 and PEG 8000.

bands at 3287 cm^{-1} and 2926 cm^{-1}, assigned to O–H stretching from adsorbed water and/or hydroxyl groups, as well as possible residual organic species from the soft-template synthesis. The band at 1626 cm^{-1} corresponds to the H–O–H bending mode of molecular water, suggesting hydration within or on the particle surfaces. Additional bands at 1455, 1353, and 1241 cm^{-1} may be attributed to C–H bending and C–O stretching vibrations, indicating the presence of a small amount of residual organic compounds originating from the DEG or PEG solvents. In contrast, the nanorod and nanoparticle samples show a marked reduction or absence of the high-frequency bands near 3287 and 2926 cm^{-1}. This indicates a lower concentration of surface-bound water and organic residues compared to the nanowires. This confirms that the soft-template agents PEG and DEG were almost completely removed after the sample washing process.

3.2. Optical properties

The photoluminescence excitation (PLE) spectrum of $GdPO_4{\cdot}H_2O{:}Tb^{3+}$is monitored at the dominant 543 nm emission ($^5D_4 \rightarrow {}^7F_5$). Figure 7 shows the characteristic excitation bands of $GdPO_4{\cdot}H_2O{:}Tb^{3+}$ from both the host Gd^{3+} and the activation Tb^{3+} ions. The narrow, sharp bands associated with Gd^{3+} ions are observed at 272 nm ($^8S_{7/2} \rightarrow {}^6I_{11/2}$), 275 nm ($^8S_{7/2} \rightarrow {}^6I_{9/2}$) 277 nm ($^8S_{7/2} \rightarrow {}^6I_{7/2}$), 305 nm ($^8S_{7/2} \rightarrow {}^6P_{5/2}$), and 310 nm ($^8S_{7/2} \rightarrow {}^6P_{7/2}$). Direct excitation of the Tb^{3+} ions is observed at 350 nm ($^7F_6 \rightarrow {}^5D_2$), 367 nm ($^7F_6 \rightarrow {}^5L_{10}$), and 377 nm ($^7F_6 \rightarrow {}^5D_6$), arising from intra-4f electronic transitions [28–31]. The simultaneous observation of the $Gd_3{}^+$ absorption bands in the excitation spectrum recorded at the Tb^{3+} emission wavelength provides clear evidence of the $Gd_3{}^+ \rightarrow Tb^{3+}$ energy transfer. This mechanism involves Gd^{3+} ions acting as sensitizers and Tb^{3+} ions serving as activators. Therefore, the simultaneous presence of both Gd^{3+} and Tb^{3+} absorption bands in the excitation spectrum constitutes direct spectroscopic evidence of the $Gd^{3+} \rightarrow Tb^{3+}$ energy transfer process within the $GdPO_4$ host lattice.

Based on this excitation spectrum, photoluminescence (PL) spectra of the synthesized samples were recorded under 355 nm laser diode excitation (Fig. 8). The PL spectra of the

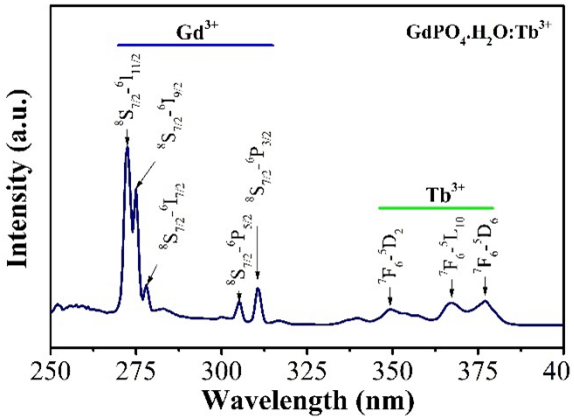

Fig. 7. Excitation spectra of $GdPO_4{\cdot}H_2O:Tb^{3+}$ sample, monitored at the dominant 543 nm emission.

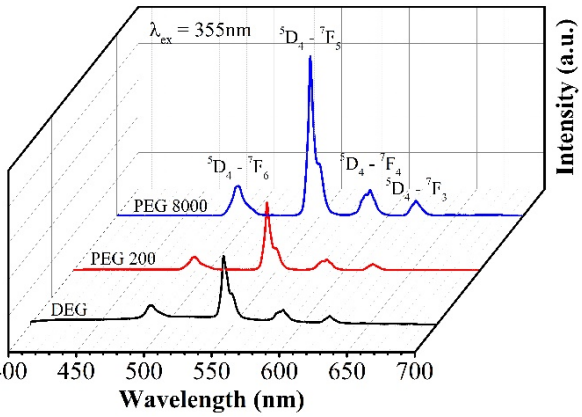

Fig. 8. Fluorescence spectra of $GdPO_4{\cdot}H_2O:Tb^{3+}$ samples with different solvents DEG, PEG 200 and PEG 8000 under 355 nm excitation.

$GdPO_4 \cdot H_2O:Tb^{3+}$ synthesized via a solvothermal method with DEG, PEG 200, and PEG 8000 as soft templates exhibit four prominent emission bands corresponding to the characteristic transitions of Tb^{3+}, which are located at 489 nm ($^5D_4 \rightarrow {}^7F_6$), 543 nm ($^5D_4 \rightarrow {}^7F_5$), 586 nm ($^5D_4 \rightarrow {}^7F_4$), and 620 nm ($^5D_4 \rightarrow {}^7F_5$). Among these, the green emission at 543 nm ($^5D_4 \rightarrow {}^7F_5$) is dominant, confirming efficient Tb^{3+} emission in the prepared phosphors. The highest PL intensity was obtained from the PEG 8000-mediated nanoparticles, followed by PEG 200-mediated nanorods and DEG-mediated nanowires. The observed morphology-dependent variation in luminescence intensity is likely a consequence of changes in the material's effective surface area and the resulting light–matter interaction efficiency. However, further in-depth studies are warranted to quantitatively confirm and fully elucidate this complex relationship.

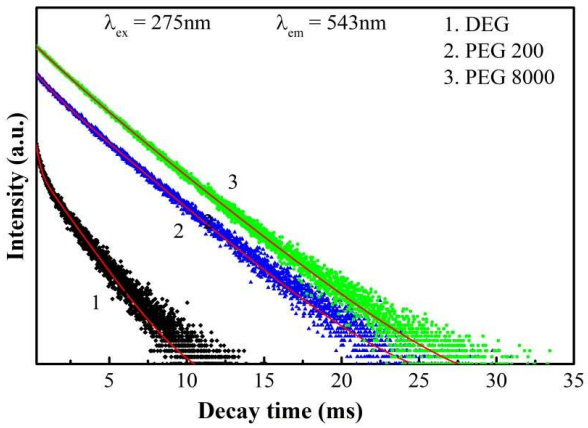

Fig. 9. Luminescence lifetime of $GdPO_4{\cdot}H_2O:Tb^{3+}$ samples with different solvents DEG, PEG 200 and PEG 8000 under excitation at 275 nm.

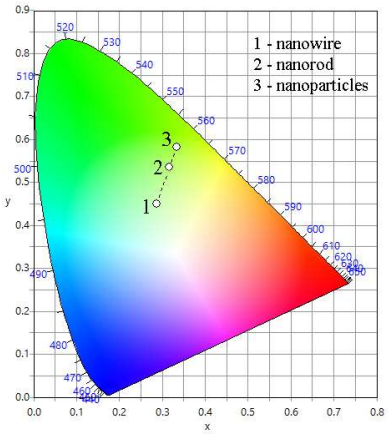

Fig. 10. CIE chromaticity diagram of the emission spectra for $GdPO_4 \cdot H_2O:Tb^{3+}$ in nanowire, nanorod, and nanoparticle morphologies.

Fluorescence lifetime: The fluorescence lifetime is a critical parameter that quantifies a material's luminescence efficiency and provides key insight into the kinetics of energy transfer and relaxation processes. The fluorescence lifetime (decay) is defined as the time required for the number of ions in the excited state to decrease to $1/e$ of its initial value after the excitation source is terminated [13, 29]. Fig. 9 illustrates the decay curves for the characteristic $^5D_4 \rightarrow {}^7F_5$ emission ($\lambda_{e_m} = 543$ nm), obtained under 275 nm excitation for the $GdPO_4 \cdot H_2O{:}Tb^{3+}$ samples. All the decay curves were well fitted using a bi-exponential function described by the equation:

$$I = A_1 \exp(-t/\tau_1) + A_2 \exp(-t/\tau_2),$$

where, I is the fluorescence intensity at time t. A_1, A_2 are fitting parameters, τ_1 and τ_2 are the short and long decay components, respectively. The average lifetime (τ_{avg}) is calculated by the following formula:

$$\tau_{avg} = \frac{\sum(Ai \times \tau i)}{\sum Ai}.$$

The measured average lifetimes exhibit a clear dependence on morphology, increasing in the order: nanowire (τ= 2.615 ms), rod-shaped (τ= 3.316 ms), nanoparticle (τ= 3.464 ms). The longest lifetime observed for the nanoparticle sample synthesized using PEG 8000 directly indicates the lowest non-radiative loss rate and, consequently, the highest radiative probability. The quantitative findings provide strong support for the correlation between enhanced photoluminescence efficiency and the material's refined nanoparticle morphology.

Table 2. Decay time fitting parameters and average fluorescence lifetimes of DEG, PEG 200, and PEG 8000.

	DEG	PEG 200	PEG 8000
A1	657	765	4849
τ_1 (ms)	3.212	0.901	3.801
A2	740	3226	2174
τ_2 (ms)	1.378	3.465	2.126
Average lifetime (ms)	**2.615**	**3.316**	**3.464**
Goodness of fit (R^2)	0.9830	0.9991	0.9996

As shown in Table 2, the decay time fitting exhibited excellent agreement between the experimental data and the fitted curves, with a goodness of fit (R^2) of approximately 0.99, demonstrating the high quality of the fit.

Color Coordinate Analysis: The CIE (Commission International de L'Eclairage) chromaticity coordinates were calculated from the emission spectra of the $GdPO_4{\cdot}H_2O{:}Tb^{3+}$ nanostructures to precisely locate their emission color and evaluate any hue shifts (Fig. 10). Analyzing these coordinates provides insight into how the structural, morphology, and local crystal field environment of the Tb^{3+} ions influence the material's optical properties. Under 355 nm excitation, the (x, y) chromaticity coordinates for the three distinct morphologies exhibited clear variations in emission hue. Specifically, the wire-shaped sample showed coordinates of (0.33, 0.58), positioned in the yellow–green region of the CIE diagram, indicating a considerable contribution from the yellow emission lines ($^5D_4 \rightarrow {}^7F_4$, ~585 nm) in addition to the characteristic green emission ($^5D_4 \rightarrow {}^7F_5$, ~545 nm). The rod-shaped sample, with coordinates of (0.32, 0.53), shifted toward the

pure green region, suggesting that its emission is more predominantly governed by the $^5D_4 \rightarrow ^7F_5$ transition, with a reduced yellow component compared to the nanowires. In contrast, the particle-shaped sample exhibited coordinates of (0.28, 0.45), located near the cyan–green region, reflecting a cooler emission hue due to an enhanced short-wavelength component. The observed shifts in chromaticity coordinates across the different morphologies highlight the crucial role of particle shape and size in modulating the local environment around Tb^{3+} ions. This directly affects the relative intensities of the characteristic emission transitions. These findings not only provide evidence for morphology-dependent photoluminescence mechanisms but also demonstrate a simple and effective method for deliberately tuning emission colors. This capability opens up the potential for morphology engineering to design phosphor materials with tailored emission colors, which is highly desirable for next-generation solid-state lighting and display technologies.

4. Conclusion

In this study, we successfully synthesized $GdPO_4 \cdot H_2O:Tb^{3+}$ nanostructures with tunable morphologies using a solvent-mediated solvothermal method. By systematically varying the solvent, we demonstrated a direct link between solvent type and resulting morphology: DEG, PEG 200, and PEG 8000 produced nanowires, nanorods, and nanoparticles, respectively. Zeta potential analysis revealed that the PEG 8000-mediated nanoparticles exhibited good colloidal stability in aqueous solutions (-35 mV). Photoluminescence studies showed that these nanoparticles also produced the highest green emission intensity at 543 nm ($^5D_4 \rightarrow ^7F_5$). The PL decay curves of the characteristic $5D_4 \rightarrow 7Fs$ transition ($\lambda_{ex} = 275$ nm, $\lambda_{e_m} = 543$ nm) revealed a pronounced morphology-dependent lifetime enhancement, rising from 2.615 ms (nanowires, DEG-synthesized) to a maximum 3.464 ms (nanoparticles, PEG 8000-synthesized), indicating a higher radiative probability and reduced non-radiative losses for the nanoparticle morphology. These findings highlight a simple and effective strategy for tailoring both the morphology and optical performance of $GdPO_4$-based phosphors. This approach provides a valuable pathway for optimizing these materials for future applications in advanced photonic, sensing, and bioimaging technologies.

Acknowledgements

This research is funded by Vietnam Academy of Science and Technology, under grant number KHCBVL.02/23-24. The authors gratefully acknowledge Laboratory of Photochem, Photonics and Imaging, and National Key Laboratory for Electronic Materials and Devices, Institute of Materials Science, for their support.

Authors contributions

Nguyen Thanh Huong conceived the research, designed the experiments, supervised the project, and drafted the manuscript. Pham Thi Lien conducted material synthesis and data processing. Hoang Thi Khuyen performed TEM/SEM measurements and image analysis. Nguyen Thi Ngoc Anh analysed the data and revised the manuscript. Do Khanh Tung carried out structural characterizations and interpreted the results. Nguyen Vu performed optical measurements and data analysis. Dinh Manh Tien conducted Raman and FTIR analyses and assisted with reference management. Nguyen Thanh Binh contributed to manuscript editing.

Conflict of interest

The authors declare no known competing financial or personal interests that could have influenced the work reported in this paper.

References

[1] Q. Zhang, S. O'Brien and J. Grimm, *Biomedical applications of lanthanide nanomaterials for imaging, sensing and therapy*, Nanotheranostics **6** (2022) 184.

[2] X. Luo, C. Zhang, Z. Yu, S. Wen and Y. Xian, *Recent advances in responsive lanthanide-doped luminescence nanoprobes in the near-infrared-II window*, TrAC, Trends Anal. Chem. **169** (2023) 117368.

[3] S. V. Eliseeva and J.-C. G. Bünzli, *Lanthanide luminescence for functional materials and bio-sciences*, Chem. Soc. Rev. **39** (2010) 189.

[4] S. Faulkner, S. J. A. Pope and B. P. Burton-Pye, *Lanthanide complexes for luminescent imaging applications*, Appl. Spectrosc. Rev. **40** (2005) 1.

[5] S. K. Nethi, V. S. Bollu, N. A. Anand and C. R. Patra, *Rare earth-based nanoparticles: Biomedical applications, pharmacological and toxicological significance*, in *Nanoparticles and their Biomedical Applications*, p. 1, (2020).

[6] Z. Yu, C. Eich and L. J. Cruz, *Recent advances in rare-earth-doped nanoparticles for NIR-II imaging and cancer theranostics*, Front. Chem. **8** (2020) 496.

[7] J.-H. Choi, G. Fremy, T. Charnay, N. Fayad, J. Pécaut, S. Erbek *et al.*, *Luminescent peptide/lanthanide(III) complex conjugates with push–pull antennas*, Inorg. Chem. **61** (2022) 20674.

[8] T. Guo, Y. Zhang, Q. Zhao, C. Wang, M. Du, Z. Xia *et al.*, *Development status of rare earth luminescence material*, J. Alloys Compd. **1037** (2025) 182399.

[9] X. Pan, Y. Jian, N. An, R.-J. Xie, S. Ke, Z. Li *et al.*, *Innovations in phosphate phosphors*, Coord. Chem. Rev. **528** (2025) 216407.

[10] D. Chávez-García and M. Guzman, *Upconversion luminescent nanoparticles and their biomedical applications in imaging*, in *Luminescence: Basic Concepts and Emerging Applications*, p. 1005378, IntechOpen, (2024).

[11] D. Budrevičius, N. Kajimoto, A. Pakalniškis, K. Tsuru, A. Kareiva and R. Skaudžius, *Improvement of luminescent properties of GdPO4:Eu by La co-doping*, Ceram. Int. **49** (2023) 2373.

[12] M. Hasegawa, H. Ohmagari, H. Tanaka and K. Machida, *Luminescence of lanthanide complexes*, J. Photochem. Photobiol. C **50** (2022) 100484.

[13] Q. Wang, J. Wu, B. Wu, H. Jia, Y. Zhang, Z. Liu *et al.*, *Construction of a nanofluorescent probe* $GdPO_4 \cdot H_2O{:}Tb@GdPO_4@PEG$, Ceram. Int. **50** (2024) 38841.

[14] Z. Guo, J. Liu, M. Lv, S. Wang, F. Li, T. Xu *et al.*, *Organic molecule-mediated synthesis of* $GdPO_4{:}Eu$, Ceram. Int. **51** (2025) 1042.

[15] E. C. Lewandowski, C. B. Arban, M. P. Deal, A. L. Batchev and M. J. Allen, *Europium(II/III) coordination chemistry toward applications*, Chem. Commun. **60** (2024) 10655.

[16] P. T. Lien, N. T. Huong, T. T. Huong, H. T. Khuyen, N. T. N. Anh, N. D. Van *et al.*, *Optimization of* Tb^{3+}/Gd^{3+} *molar ratio for rapid detection of naja atra cobra venom by immunoglobulin g-conjugated* $GdPO_4.nH_2O{:}Tb^{3+}$ *nanorods*, J. Nanomater. **2019** (2019) 3858439.

[17] D. D. Yengkhom, G. S. Ningombam, R. Heisnam, N. Sharma, R. S. Nongmaithem and F. A. S. Chipem, *Carboxymethylcellulose modified* $Fe_3O_4@SiO_2@GdPO_4{:}Tb,Ce$ *nanocomposites for combined optical and magnetic fluid hyperthermia in cancer therapy*, RSC Appl. Interfaces **1** (2024) 313.

[18] H. T. Phuong, T. T. Huong, L. T. Vinh, H. T. Khuyen, D. T. Thao, N. T. Huong *et al.*, *Synthesis and characterization of* $NaYF_4{:}Yb_3{}^+,Er_3{}^+@silica\text{-}n{=}folic$ *acid nanocomplex for bioimaginable detecting MCF−7 breast cancer cells*, J. Rare Earths **37** (2019) 1183.

[19] S. Mondal, V. T. Nguyen, S. Park, J. Choi, T. M. T. Vo, J. H. Shin *et al.*, *Rare-earth-doped hydroxyapatite luminescent bioceramics*, Ceram. Int. **46** (2020) 29249.

[20] T. K. Anh, T. T. Huong, N. T. Huong, V. T. T. Ha, D. V. Thai, W. S. Strek *et al.*, *Upconversion luminescence properties of* $Gd_2O_3{:}Er$ *nanospheres*, Mater. Trans. **61** (2020) 1569.

[21] L. Tong, J. Cao, K. Wang, J. Song and J. Mu, *Lanthanide-doped nanomaterials for tumor diagnosis and treatment by second near-infrared fluorescence imaging*, Adv. Opt. Mater. **12** (2023) 2301767.

[22] P. T. Lien, V. D. Tu, L. N. Diep, N. T. Huong, H. T. Khuyen, N. T. N. Anh *et al.*, *Gd_2O_3:Eu nanocomplexes conjugated with igg for CEA detection*, Mater. Trans. **61** (2020) 1575.
[23] H. Li, H. Liu, K.-L. Wong and A. H. All, *Lanthanide-doped upconversion nanoparticles as nanoprobes*, Biomater. Sci. **12** (2024) 4650.
[24] S. Ullah, Y. Feng, M. Zhu, H. Kong, S. Sun, C. Dou *et al.*, *(GdxLa$_1$ –x)PO_4:Eu orange-red emitting phosphors*, J. Mater. Sci. Mater. Electron. **30** (2019) 14703.
[25] Z. Wang, Y. Tang, D. Fan, X. Liu, Y. Wang and J.-G. Li, *(Gd, Eu)PO_4 urchin-like hollow spheres*, J. Alloys Compd. **824** (2020) 153809.
[26] T. Gholami, H. Seifi, E. A. Dawi, M. Pirsaheb, S. Seifi, A. M. Aljeboree *et al.*, *Effect of solvent on the synthesis and morphology of nanostructures*, Mater. Sci. Eng. B **304** (2024) 117370.
[27] S. Chong, B. J. Riley, X. Lu, J. Du, T. Mahadevan and V. Hegde, *Anhydrous rare-earth phosphates: A review*, RSC Adv. **14** (2024) 18978.
[28] X. Meng, L. Zhang, C. Zhong, Y. Ruan, Y. Lv, J. Liu *et al.*, *Enhanced photoluminescence and energy transfer of Li^+ Co-doped $GdPO_4.H_2O$:Tb,Ce green phosphors*, Ceram. Int. **51** (2025) 25169.
[29] Q. Wang, J. Wu, B. Wu, Z. Liu, Y. Hu, X. Zhang *et al.*, *Morphology and fluorescence properties of $GdPO_4.H_2O$:Tb*, Mater. Res. Bull. **170** (2024) 112565.
[30] J. Yang, X. Wang, L. Song, N. Luo, J. Dong, S. Gan *et al.*, *Tunable luminescence of $GdPO_4 \cdot H_2O$:Tb,Eu nanocrystals*, Opt. Mater. **85** (2018) 71.
[31] J. Tian, F. Zhang, Y. Han, X. Zhao, C. Chen, C. Zhang *et al.*, *Multifunctional $GdPO_4$ hierarchical hollow spheres*, Appl. Surf. Sci. **475** (2019) 264.